Supplementary information:
A Compact and Effective Photon-Resolved Image Scanning Microscope

Giorgio Tortarolo[a,e,§], **Alessandro Zunino**[a,§], **Simonluca Piazza**[a,d], **Mattia Donato**[a], **Sabrina Zappone**[a,c], **Agnieszka Pierzyńska-Mach**[b], **Marco Castello**[a,d,*], **Giuseppe Vicidomini**[a,*]

[a]Istituto Italiano di Tecnologia, Molecular Microscopy and Spectroscopy, Via Enrico Melen, 83, Genoa, Italy, 16152
[b]Istituto Italiano di Tecnologia, Nanoscopy and NIC@IIT, Via Enrico Melen, 83, Genoa, Italy, 16152
[c]University of Genoa, Dipartimento di Informatica, Bioingegneria, Robotica e Ingegneria dei Sistemi, Via Dodecaneso 35, Genoa, Italy, 16146
[d]Genoa Instruments, Via Enrico Melen, 83, Genoa, Italy, 16152
[e]Current affiliation: École Polytechnique Fédérale de Lausanne, Laboratory of Experimental Biophysics, Route de la Sorge, Lausanne, Switzerland, 1015

*Marco Castello, marco.castello@genoainstruments.com; Giuseppe Vicidomini, giuseppe.vicidomini@iit.it
§These authors contributed equally to this work

1 DFD - Theory and implementation

1.1 Working principle of heterodyne acquisition

The core idea of the DFD acquisition is to sample a periodic event at a slightly different periodicity, accumulating signal across multiple periods. Such heterodyne measurement results in the cross-correlation between the sampling window and the event, sampled at a higher rate than it would have been possible with conventional sampling. Indeed, by properly tuning the measurement parameters, the effective time step can be much shorter than the actual duration of the sampling window.

We now analyze the DFD working principle in detail. We excite the fluorescence emission by exciting the fluorophores at the excitation frequency f_{exc}. Then, we impose the sampling frequency f_s to be slightly detuned from the excitation. The cross-correlation frequency f_c is the beating frequency between the sampling and excitation frequency:

$$f_c = f_s - f_{exc} \tag{1}$$

where we assumed $f_s > f_{exc}$. Then, we impose f_s to be an integer multiple of f_c

$$f_s = k f_c \qquad k \in \mathbb{N} \tag{2}$$

and we define a windowing frequency f_w to be a multiple integer of f_s

$$f_w = n f_s \qquad n \in \mathbb{N} \tag{3}$$

Using the equations above, we find the relation of f_{exc} with f_w and f_s

$$f_{exc} = \frac{k-1}{k} f_s = \frac{k-1}{nk} f_w \tag{4}$$

Therefore, the cross-correlation period contains an integer number of excitation and sampling periods

$$T_c = (k-1)T_{exc} = kT_s = knT_w \tag{5}$$

In other words, the excitation and sampling signal are in phase every T_c, which is the periodicity of the DFD measurement.

To calculate the arrival time of the detected photons, we define the following counters

$$w \in [0, n) \tag{6}$$

$$\varphi \in [0, k) \tag{7}$$

The counter w indicates the window of the arrival time, inside a sampling period. The counter φ indicates the phase delay between the sampling and excitation signal. Thus, the sampling time with respect to the excitation is

$$t = \varphi(T_s - T_{exc}) + wT_w \tag{8}$$

The first term represents the delay between excitation and sampling periods (the time interval between the dashed line and the following exponential decay, in Fig. 1b). The second term represents a time advancement, given by the position of the sampling windows with respect to the sampling clock (the time interval between the dashed line and the window with index w, in Fig. 1b). It is useful to rewrite the above equation using a single period as the unit of time

$$t = T_w\left(w - \varphi\frac{n}{k-1}\right) \tag{9}$$

Note that we are sampling a signal with period $T_{exc} = T_w \cdot \frac{kn}{k-1}$. Thus, we take the remainder of the division of the time delay to the period of the signal. Normalizing the result by T_w, we get the following dimensionless index

$$\gamma = f_w(t \bmod T_{exc}) = \left(w - \varphi\frac{n}{k-1}\right) \bmod \left(\frac{kn}{k-1}\right) \tag{10}$$

it is useful to multiply both operands by $(k-1)$ to get an integer index

$$\gamma = [(k-1)w - \varphi n] \bmod (nk) \tag{11}$$

which ranges from 0 to $nk-1$. The corresponding photon arrival time is

$$t = \frac{T_{exc}}{nk}\{[(k-1)w - \varphi n] \bmod (nk)\} \tag{12}$$

The above equation enables us to sample the excitation period with a step of $\Delta t = \frac{T_{exc}}{nk}$. However, in a practical scenario, it could be desirable to trade temporal precision for additional photon counts per time bin. To achieve this goal, we require the windowing period to be an integer multiple of the delay between excitation and sampling periods

$$T_w = m \cdot (T_s - T_{exc}) \qquad m \in \mathbb{N} \tag{13}$$

The above condition implies

$$\frac{k-1}{n} = m \in \mathbb{N} \tag{14}$$

If the above condition applies, then equation 11 can be rewritten as

$$\gamma = [n(mw - \varphi)] \bmod (nk) \tag{15}$$

Notably, the time indices can now only be multiples of n. In other words, the sampling step is now $\Delta t = \frac{T_{exc}}{k}$. Thus, we further simplify the time index by dividing both operands by n

$$\gamma = (mw - \varphi) \bmod k \tag{16}$$

Each index calculated with the above equation is repeated n times. Thus, we traded the sampling step size of a factor of n to gain the same factor in terms of photon counts. The obtained redundancy comes from the fact that now that the full sampling is repeated n times in the T_c period. In other words, the DFD period is now decreased to T_c/n.

Assuming that $k \gg 1$, we finally obtain

$$\gamma = \left(\frac{kw}{n} - \varphi\right) \bmod k \tag{17}$$

which takes integer values from 0 to $k-1$. The time index can be reconverted into a time value, knowing that the time interval spans an excitation period. Namely, the photon arrival time is

$$t = \frac{T_{exc}}{k}\left[\left(\frac{kw}{n} - \varphi\right) \bmod k\right] \tag{18}$$

Shifting the photon arrival time index by one window length might be desirable for visualization purposes. Thus, equation 11 becomes

$$\gamma = [(k-1)(w+1) - \varphi n] \bmod (nk) \tag{19}$$

1.2 Time-Resolved Multi-Channel Data Acquisition System

We upgraded our previously reported acquisition and controlling platform[1] with a multi-channel Digital Frequency Domain (DFD) architecture. The platform is built by two main units: (i) a real-time data-acquisition and controlling module written in LabView FPGA, implemented on a commercially available FPGA board (NI USB-7856R from National Instruments), and (ii) a module running on the host computer, for the user interface and data input-output.

The main tasks of the real-time FPGA platform are to control all the components of the microscope (i.e., lasers, galvanometric mirrors and piezo-electric stage) and to acquire the 25 digital signals from the SPAD array with a temporal precision of up to $400\,\mathrm{ps}$. The platform controls the galvanometric mirrors and the z-axis piezoelectric stage with analog voltage signals. The platform also triggers the excitation and STED pulses through digital signals. Notably, the user can freely define an excitation laser sequence of up to four excitation events per cycle from up to four excitation lasers (in this work, we used up to two excitation lasers and one STED laser). Our design enables a straightforward Pulsed Interleaving Excitation (PIE) implementation. The most significant task of the real-time module is to acquire all the signals from the SPAD array detector with a

sub-nanosecond temporal resolution. To this aim, we exploited the DFD principle, leveraging the real-time capabilities of the FPGA technology.[2]

Implementation	f_{exc} [MHz]	f_s [MHz]	k	n	T_w [ns]	Δt [ps]
20 MHz	21	21.18	120	24	1.97	397
40 MHz	39.33	40	60	12	2.08	424

Table 1 DFD parameters.From left to right: excitation frequency, sampling frequency, number of sampling periods per cross-correlation cycle, number of windows per sampling period, duration of the sampling window, and the width of the sampling step.

For ease of implementation, we chose the ratio k/n to be an integer. Therefore, the term kw/n in equation 17 can be replaced by a single counter with step k/n. More in detail, we used two combinations of parameters, that we refer to as the $20\,\mathrm{MHz}$ and the $40\,\mathrm{MHz}$ implementations. The chosen parameters can be seen in Table 1, and in both cases, we obtain a sampling step of $\Delta t = T_{exc}/k \approx 400\,\mathrm{ps}$. At the FPGA level, the platform implements a Single-Cycle Timed Loop (SCTL), running at $f_{SCTL} = 12 f_{exc}$, to generate the TTL signals to trigger up to four lasers. Independently, the data acquisition loop monitors the 25 signals from the SPAD array detector at a frequency $f_w = n f_s$. Each time a photon hits a given sensitive element, the data acquisition loop detects the rising edge of the corresponding TTL signal and increments the correct cross-correlation histogram bin accordingly, accounting the phase relation between the sampling and the excitation frequencies thanks to the phase counter φ.

The design choice to generate all the frequencies needed from the same FPGA oscillator implies the compatibility of our platform only with lasers that can be triggered externally. Although this strategy may limit our implementation in its current version, it also results in a significantly simplified controlling architecture, since it does not rely on external signals from the laser sources. Thus, no phase-locking circuits are needed. Additionally, the use of a single oscillator to generate all the frequencies increases the robustness of the platform. However, it does not allow to set the phase relation for the two frequencies at the beginning of the measurement. Indeed, one would like to start every measurement in the same phase condition – e.g., the rising edges of both f_{SCTL} and f_w being simultaneous – since the value of the phase index φ is always set to 0 for the first sampling period. In reality, this condition is not met, and multiple measurements produced at the same experimental conditions are not temporally aligned. To address this problem, we decided to implement an additional virtual data channel. We measure a digital signal provided by the FPGA itself at the frequency f_{exc}, sampled by the same SCTL accounting for the real signals from the SPAD array. Since its temporal position depends solely on the initial phase relation between f_{SCTL} and f_w, it provides a reference for registering different measurements.

At the end of each pixel dwell time, the cross-correlation histograms for each sensitive element of the detector are sent to the host computer *via* the USB 2.0 connection and are saved by a dedicated LabView module on a binary file. The chosen communication protocol consists of 16 bits per each cross-correlation histogram bin per each channel. Such protocol enables high-photon flux regimes but sets a lower limit for the duration of the dwell time to avoid data loss (in typical conditions, $125\,\mu\mathrm{s}$). It is important to highlight that this limitation is purely technical and mostly related to the communication bus equipped with the FPGA card. Indeed, implementing the firmware on more recent FPGA platforms (e.g., equipped with Thunderbolt 3 cards) would result in a performance boost up to $80\times$ in data transfer, *de facto* solving the dwell time limitation. Moreover,

the negative exponential nature of the fluorescence decay suggests the potential implementation of an adaptive communication protocol, which could use different time indices, shortening the minimum pixel dwell time. Another alternative could be to calculate the phasor coordinates at the FPGA level, reducing the data transfer load. However, this choice comes at the cost of losing the information on the high harmonics. Thus, in the current implementation, we preferred versatility over speed.

2 Description of fluorescence dynamics in time and frequency

2.1 Lifetime description in the time domain

Following the previous description of the histogram formation with the DFD approach, the fluorescence lifetime histogram $f(t)$ can be written as

$$f(t) = d(t) \star w(t) \tag{20}$$

where $\star$ denotes the cross-correlation operator. The fluorescence signal $d(t)$ is defined as follows

$$d(t) = d_0 \exp\left(-t/\tau\right) \cdot \theta(t) \tag{21}$$

where $\theta(t)$ the Heaviside step function and τ the fluorescence lifetime. The sampling window $w(t)$ is defined as follows

$$w(t) = \begin{cases} 1 & \text{if } 0 < t < T_w \\ \\ 0 & \text{otherwise} \end{cases} \tag{22}$$

where T_w is the width of the sampling window.

Using the model above, we can analytically compute the cross-correlation

$$f(t) = \int_{\mathbb{R}} d(t') \cdot w(t+t')\,\mathrm{d}t' = \begin{cases} 0 & \text{if } t \leq -T_w \\ \\ d_0 \cdot \tau \cdot \left(1 - e^{-\frac{T_w}{\tau}} \cdot e^{-\frac{t}{\tau}}\right) & \text{if } -T_w \leq t \leq 0 \\ \\ d_0 \cdot \tau \cdot \left(1 - e^{-\frac{T_w}{\tau}}\right) \cdot e^{-\frac{t}{\tau}} & \text{if } t \geq 0 \end{cases} \tag{23}$$

Notably, the result for $t \geq 0$ is still an exponential decay with unaltered lifetime, rescaled by a term that depends on τ and T_w. The scale factor is

$$\tau \cdot \left(1 - e^{-\frac{T_w}{\tau}}\right) \sim \begin{cases} T_w & \text{if } \tau \gg T_w \\ \\ \tau & \text{if } \tau \ll T_w \end{cases} \tag{24}$$

Namely, the contrast of the fluorescence signal linearly deteriorates for decays faster than the sampling window. Instead, the contrast of decays slower than the sampling window is approximately constant.

2.2 *Lifetime description in the frequency domain*

Exponential decays are conveniently analyzed in Fourier space. We consider the case of a single exponential

$$d(t) = d_0 \exp\left(-t/\tau\right) \cdot \theta(t) \tag{25}$$

with fluorescence lifetime τ. The Fourier transform of the normalized signal is

$$\frac{\mathcal{F}\{d(t)\}\,(\omega)}{\int_0^{+\infty} d(t)\,\mathrm{d}t} = \frac{1}{1+i\omega\tau} = \underbrace{\frac{1}{1+(\omega\tau)^2}}_{g(\omega)} - i\,\underbrace{\frac{\omega\tau}{1+(\omega\tau)^2}}_{s(\omega)} \tag{26}$$

where we defined $g(\omega)$ and $s(\omega)$ respectively as the real and imaginary part of the Fourier transform of the decay. Notably, these quantities are related by the following equation

$$\left[g(\omega) - 1/2\right]^2 + s^2(\omega) = 1/4 \tag{27}$$

The vector $\mathbf{p} = (g, s)$ is known as phasor and lies on the semicircle of the complex plane described by the above equation, commonly named the *universal circle*. This fact implies that the phasors of single exponential decays are bound to lie on the universal circle. Multi-exponential decays are linear combinations of single exponential decays and their corresponding phasors lie within the universal circle.

From equation 26, it is possible to calculate the lifetime in two ways. By defining

$$\tan\left[\phi(\omega)\right] = \frac{s(\omega)}{g(\omega)} \tag{28}$$

$$m^2(\omega) = s^2(\omega) + g^2(\omega) \tag{29}$$

we have that

$$\tau_\phi = \frac{1}{\omega}\tan\left[\phi(\omega)\right] \tag{30}$$

$$\tau_m = \frac{1}{\omega}\sqrt{\frac{1}{m^2(\omega)} - 1} \tag{31}$$

Note that – for single exponential decays – the two lifetime values are identical and do not depend on the frequency ω.

Sampled data are inherently discrete. Thus, we need to generalize our analysis by writing the phasor coordinates as the real and imaginary part of the discrete Fourier transform (DFT) of the sampled signal:

$$g(h) = \frac{1}{I}\sum_{p=0}^{n_p-1} d(p)\cos(2\pi hp/n_p), \tag{32}$$

$$s(h) = \frac{1}{I}\sum_{p=0}^{n_p-1} d(p)\sin(2\pi hp/n_p), \tag{33}$$

where $I = \sum_p d(p)$ and n_p is the number of data points. Identifying $\omega = 2\pi h f_{\text{exc}}$, the fluorescence lifetime values are the following

$$\tau_\phi = \frac{1}{2\pi h f_{exc}}\tan\left[\phi(h)\right] \tag{34}$$

$$\tau_m = \frac{1}{2\pi h f_{exc}}\sqrt{\frac{1}{m^2(h)} - 1}. \tag{35}$$

Importantly, phasors can be calculated at any discrete frequency h. However, low frequencies carry most of the signal. As such, a typical choice is $h = 1$, commonly referred to as the first harmonic.

All the data analysis presented in this work is performed leveraging a custom-written Matlab application, hosting a graphical user interface to load and manipulate the raw data files generated by the LabView module, taking full advantage of the phasors representation for time-resolved measurements.

2.3 Calibration of the DFD acquisition platform

In order to retrieve the correct lifetime values from the time-resolved measurements, it is necessary to calibrate the effect of the instrument response on the measurement. Indeed, in a realistic scenario, the impulse response function (IRF) of the microscope is

$$h(t) = w(t) * p(t) * j(t) \tag{36}$$

where $*$ denotes the convolution operator, $w(t)$ is the DFD sampling window, $p(t)$ is the envelope of the excitation laser pulse, and $j(t)$ is the jitter of the detection system. Thus, we can write the fluorescence lifetime histogram $f(t)$ as

$$f(t) = d(t) * h(t) \tag{37}$$

where $d(t)$ is the fluorescence signal and $h(t)$ is the IRF of the system. In Fourier space, the same relation can be rewritten using the convolution theorem

$$F(\omega) = D(\omega) \cdot H(\omega) \tag{38}$$

Fixing a single frequency (the one chosen for the phasor calculation) and writing the functions in the exponential form, we have

$$F = m_F e^{i\phi_F} = (m_D \cdot m_H)\exp\left[i(\phi_D + \phi_H)\right] \tag{39}$$

We can compute the modulus m_H and the phase ϕ_H of the IRF using a sample with a known lifetime, usually a solution of a fluorophore of choice. For such calibration measurement, each of the 25 time-resolved images is integrated along the (x_s, y_s) coordinates since the temporal fluorescence behaviour and the instrument response are invariant to the scan position. The time-resolved calibration measurement yields to a set $[\phi_C(\mathbf{x}_d), m_C(\mathbf{x}_d)]$, one phasor for each SPAD element at coordinate $\mathbf{x}_d = (x_d, y_d)$. Similarly, we describe the IRF of each SPAD element as the set $[\phi_H(\mathbf{x}_d), m_H(\mathbf{x}_d)]$ in order to account for potential differences between channels (e.g., different circuitry at the detector level, resulting in different recorded delays for simultaneous photons hitting different channels). Using equations 35 and the known lifetime $\hat{\tau}$, we can calculate the modulus and phase of the phasor as follows

$$\hat{\phi} = \arctan(2\pi f_{exc}\hat{\tau}), \tag{40}$$

$$\hat{m} = \sqrt{\frac{1}{\hat{\tau}^2 + (2\pi f_{exc})^2 + 1}}, \tag{41}$$

here calculated at the first harmonic, $h = 1$. Thus, we obtain the instrument response as a rotation and a scale in the complex plane.

$$\phi_H(\mathbf{x}_d) = \phi_C(\mathbf{x}_d) - \hat{\phi} \tag{42}$$

$$m_H(\mathbf{x}_d) = m_C(\mathbf{x}_d)/\hat{m}. \tag{43}$$

Then, we use the instrument response set to calibrate all the temporal histograms at each position (x_s, y_s), finally obtaining the correct values $[\phi_D(\mathbf{x}_d), m_D(\mathbf{x}_d)]$ from the measured values $[\phi_F(\mathbf{x}_d), m_F(\mathbf{x}_d)]$

$$\phi_D(\mathbf{x}_s, \mathbf{x}_d) = \phi_F(\mathbf{x}_s, \mathbf{x}_d) - \phi_H(\mathbf{x}_d) + \varphi - \hat{\varphi} \tag{44}$$

$$m_D(\mathbf{x}_s, \mathbf{x}_d) = m_F(\mathbf{x}_s, \mathbf{x}_d)/m_H(\mathbf{x}_d), \tag{45}$$

where all the arithmetic operations are intended to be element-wise, and φ and $\hat{\varphi}$ are the phases retrieved from the additional virtual channel, respectively, for the experimental measurement and the calibration measurement. These two terms account for a non-deterministic phase relation between the excitation and the frequency sampling at the beginning of each measurement and cannot be pre-calibrated. In general, the described calibration in the phasor domain allows the retrieval of the correct lifetime values for a given measurement – by accounting for the instrument response – and to manipulate the data for a variety of operations directly in the phasor space (e.g., segmentation, decomposition, filtering). Additionally, for this work, it is also beneficial to back-propagate the calibration operation in the image space since it allows to inherently correct for the temporal differences between different channels of the SPAD array detector. The resulting "temporally aligned" images may then be fed to analysis pipelines working in the images space (such as the SPLIT-ISM pipeline).

2.4 Phasor space

The Fourier transform of a generic temporal signal $f(t)$ evaluated at the arbitrary frequency ω_0 is

$$|F(\omega_0)| = \left| \int_{\mathbb{R}} f(t) e^{-i\omega t} \, \mathrm{d}t \right| \leq \int_{\mathbb{R}} \left| f(t) e^{-i\omega t} \right| \mathrm{d}t = \int_{\mathbb{R}} |f(t)| \, \mathrm{d}t = \int_0^{+\infty} f(t) \, \mathrm{d}t \tag{46}$$

where, for the last equality, we assumed the fluorescence signal to be positive and non-zero only for $t > 0$. Using the definition of phasor from Eq. 26, we have that the magnitude of the raw phasor $\mathbf{p}$ is

$$|\mathbf{p}(\omega_0)| = \frac{|F(\omega_0)|}{\int_0^{+\infty} f(t) \, \mathrm{d}t} \leq 1 \qquad \forall \omega_0 \tag{47}$$

In other words, the phasor space is the unit circle in the complex plane.
After calibration, the magnitude of the phasor is dilated by the magnitude of the IRF. Thus, we have:

$$|\hat{\mathbf{p}}(\omega_0|\mathbf{x}_d)| \leq m_H^{-1}(\omega_0|\mathbf{x}_d) \tag{48}$$

where $\hat{\mathbf{p}}$ is the calibrated phasor. Therefore, for the FLISM phasor, the bound becomes

$$|\hat{\mathbf{p}}_{FLISM}(\omega_0)| \leq \max_{\mathbf{x}_d} \left\{ m_H^{-1}(\omega_0|\mathbf{x}_d) \right\} \tag{49}$$

To provide an estimate of m_H, we now assume the IRF to be rectangular

$$h(t) = \begin{cases} 1 & \text{if } 0 \leq t \leq T \\ 0 & \text{otherwise} \end{cases} \tag{50}$$

Therefore, we have that

$$m_H(\omega) = \frac{|H(\omega)|}{\int_0^{+\infty} h(t) \, \mathrm{d}t} = |\mathrm{sinc}(\omega T/2)| \underset{\omega T \to 0}{\sim} 1 \tag{51}$$

Namely, if $T_{\text{exc}} \gg T_w$, then m_H is close to unity.

3 Image processing

3.1 FLISM data analysis

The acquisition system generates the five-dimensional array $i(\mathbf{x}_s, \mathbf{x}_d, t)$. First, we apply the adaptive pixel reassignment (APR) algorithm[1] to generate the corresponding FLISM image. To do it, we calculate the ISM images by integrating the data over time

$$i(\mathbf{x}_s|\mathbf{x}_d) = \int i(\mathbf{x}_s, \mathbf{x}_d, t) \, \mathrm{d}t \tag{52}$$

Now, we calculate the phase correlation between the images of the ISM dataset and the one generated by the central element used as the reference

$$R(\mathbf{x}_s|\mathbf{x}_d) = \mathcal{F}^{-1}\left\{ \frac{\mathcal{F}\{i(\mathbf{x}_s|\mathbf{x}_d)\} \cdot \overline{\mathcal{F}\{i(\mathbf{x}_s|\mathbf{0})\}}}{\left|\mathcal{F}\{i(\mathbf{x}_s|\mathbf{x}_d)\} \cdot \overline{\mathcal{F}\{i(\mathbf{x}_s|\mathbf{0})\}}\right|} \right\} \tag{53}$$

where $\mathcal{F}$ and $\mathcal{F}^{-1}$ denote the Fourier transform and its inverse, respectively. We measure the shift vectors as the position of the maximum correlation

$$\boldsymbol{\mu}(\mathbf{x}_d) = \arg\max_{\mathbf{x}_s} \{R(\mathbf{x}_s|\mathbf{x}_d)\} \tag{54}$$

The FLISM image is calculated by shifting the 5D dataset by the corresponding shift-vectors

$$i_{\text{FLISM}}(\mathbf{x}_s, \mathbf{x}_d, t) = i[\mathbf{x}_s + \boldsymbol{\mu}(\mathbf{x}_d), \mathbf{x}_d, t] \tag{55}$$

Then, we apply the calibration procedure explained in section 2.3 for each coordinate $\mathbf{x}_d$. More in detail, we use the IRF phase values $\phi_H(\mathbf{x}_d)$ to align in time the 25 fluorescence decays. Then, we integrate over the detector space

$$i_{\text{FLISM}}(\mathbf{x}_s, t) = \int i[\mathbf{x}_s + \boldsymbol{\mu}(\mathbf{x}_d), \mathbf{x}_d, t - \phi_H(\mathbf{x}_d)/\omega_{exc}]\, \mathrm{d}\mathbf{x}_d \tag{56}$$

Finally, we extract a single IRF magnitude value m_H from the calibration measurement integrated over the detector space, as explained in the section 2.3. We use m_H to calibrate the corresponding FLISM phasors, calculated from the data in Eq. 56. The result is a phasor map $\mathbf{p}(\mathbf{x}_s)$, which can be converted into a lifetime map $\tau(\mathbf{x}_s)$ using Eq. 31. Integrating the FLISM dataset over time, we obtain the ISM intensity map $i(\mathbf{x}_s)$. The intensity and lifetime maps are combined together in a 2D colormap to represent the FLISM results.
The open-confocal images are obtained with the same exact procedure, with the exception that we do not apply the APR algorithm to the dataset.

3.1.1 Phasor separation

Here, we describe the algorithm we use to separate the contributions of fluorophores with different lifetimes. It consists of a linear method built on the phasor representation of time-resolved fluorescence data. It decomposes the dataset $i_{\text{FLISM}}(\mathbf{x}_s, t)$ pixel-by-pixel by calculating the phasor of the temporal component and unmixing different contributions by inverting a linear model.

For each scan coordinate $\mathbf{x}_s$, we assume that the flux of of fluorescence photons contains two components

$$i(t) = N_1 \cdot \frac{1}{\tau_1} d_1(t) + N_2 \cdot \frac{1}{\tau_2} d_2(t) \tag{57}$$

where N_1 and N_2 are the numbers of photons collected with a different lifetime and

$$d_i(t) = \theta(t - T_i) \exp(-t/\tau_i) \tag{58}$$

where $T_2 = 0$ or $T_2 = T_{exc}/2$ for synchronous or pulsed interleaving excitation, respectively. We describe each component using the phasor representation $\mathbf{p} = (g, s)$ and obtain the following

linear system

$$\mathbf{p} = \begin{pmatrix} g \\ s \end{pmatrix} = \begin{pmatrix} g_1 & g_2 \\ s_1 & s_2 \end{pmatrix} \begin{pmatrix} f_1 \\ f_2 \end{pmatrix} = f_1\mathbf{p}_1 + f_2\mathbf{p}_2 = \mathbf{M}\mathbf{f} \tag{59}$$

where each phasor $\mathbf{p}_i$ represent a single exponential decay and $f_i = \frac{N_i}{\sum_i N_i}$ are the weights that describe the corresponding fractional components. If the matrix $\mathbf{M}$ is known, it is possible to retrieve the vector of fractional components $\mathbf{f}$ from a measured phasor $\mathbf{p}$.

The linear system described by Eq. 59 solution can be simply solved as follows

$$\mathbf{f} = \mathbf{M}^{-1}\mathbf{p} \tag{60}$$

We iterate such procedure for each scan coordinate $\mathbf{x}_s$, obtaining the maps of fractional components $\mathbf{f}(\mathbf{x}_s)$. Finally, the phasor-separated images are calculated as

$$i(\mathbf{x}_s|\tau_i) = f_i(\mathbf{x}_s) \cdot \int i(\mathbf{x}_s, t)\,\mathrm{d}t \tag{61}$$

To find the entries of the matrix $\mathbf{M}$, we calculated the phasors $\mathbf{p}_1 = (g_1, s_1)$ and $\mathbf{p}_2 = (g_2, s_2)$ by measuring the fluorescence decay of two calibration samples, each with a single fluorophore. In detail, each phasor has been calculated by averaging the pixels over a scan.

3.1.2 Phasor segmentation

To implement phasor-segmentation, we considered in the phasor space the two semi-planes separated by the normal to the vector connecting $\mathbf{p}_1$ and $\mathbf{p}_2$, passing through its middle point. We then generated two images, each containing only the pixels corresponding to phasors in the first or second semi-plane, respectively.

3.2 SPLIT-STED-ISM data analysis

In order to improve STED-ISM resolution, we used the Separation by Lifetime Tuning (SPLIT) method.[3–5] Shift-vectors change upon applying the SPLIT algorithm (Suppl. Fig. 8). Thus, we first applied SPLIT to the data for each $\mathbf{x}_s$ and $\mathbf{x}_d$ coordinate, then applied APR to reconstruct a single image with enhanced resolution.

3.2.1 Separation by Lifetime Tuning

The SPLIT algorithm exploits the fluorescence dynamics to separate photons generated from the inner or outer regions of the probed region in STED microscopy. In this case, the flux of fluorescence photons is

$$i(t) = N_1 \cdot \frac{1}{\tau} d_1(t) + N_2 \cdot \frac{d_2(t)}{\tau + \tau_{\text{STED}} - e^{-T_{\text{STED}}/\tau_{\text{STED}}}} \tag{62}$$

where

$$d_1(t) = \theta(t)\exp(-t/\tau) \tag{63}$$

and

$$d_2(t) = \begin{cases} 0 & \text{if } t < 0 \\ \exp(-t/\tau_{\text{STED}}) & \text{if } 0 < t < T_{\text{STED}} \\ \exp(-T_{\text{STED}}/\tau_{\text{STED}}) \cdot \exp[-(t - T_{\text{STED}})/\tau] & \text{if } t > T_{\text{STED}} \end{cases} \tag{64}$$

τ is the unperturbed lifetime of the fluorophore, τ_{STED} is the lifetime shortened by the depletion beam, and T_{STED} is the duration of the depletion pulse. Photons emitted from the center of the probed region are unperturbed and decay slower than those originating from the periphery. To distinguish the two families of photons, we used the same procedure described in the previous section. However, in this case, the phasor describing the peripheral photons does not lie on the universal circle but on the trajectory connecting the unperturbed phasor $\mathbf{p}_1 = (g_1, s_1)$ to the coordinate $(1, 0)$. In this case, the phasor $\mathbf{p}_1 = (g_1, s_1)$ is calculated in the absence of depletion beam, and the phasor $\mathbf{p}_2 = (g_2, s_2)$ is manually chosen among the points on the STED trajectory. Thus, we can build the matrix $\mathbf{M}$ and proceed as described in the previous section.

4 Supplementary Figures

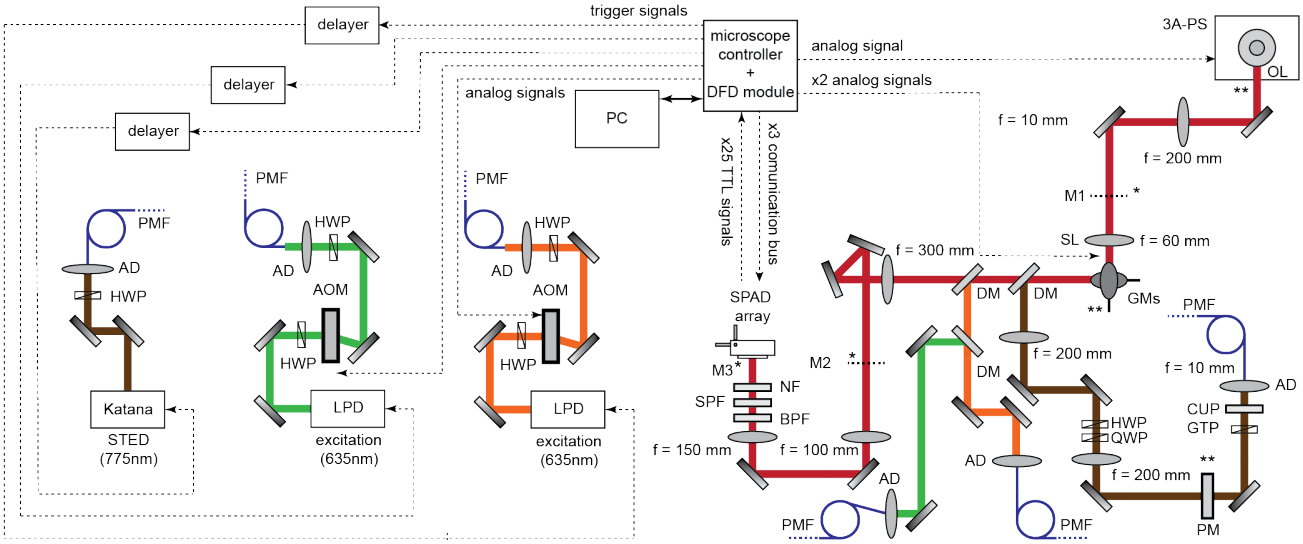

Suppl. Fig. 1 Time-resolved STED-ISM Setup. HWP: half-waveplate; QWP: quarter-wave plate; AOM: acousto-optic modulator; AD:achromatic doublet; PMF: polarized-maintaining fiber; FI: Faraday isolator; 3A-PS: three-axis piezo stage; SL: scanning lens; OL: objective lens; GMs: galvanometric mirrors; DM: dichroic mirror; BPF: band pass filter; CUP: clean-up filter; NF: notch filter; SPF: short-pass filter; APD: avalanche photo-diode; PM: phase-mask; GTP: Glan-Thompson polarizer; . Magnifications: M1 = 60×, M2 = 300×, M3 = 450×. The asterisk denotes the plane conjugate to the image plane. The double asterisks denote the plane conjugate to the objective back-aperture.

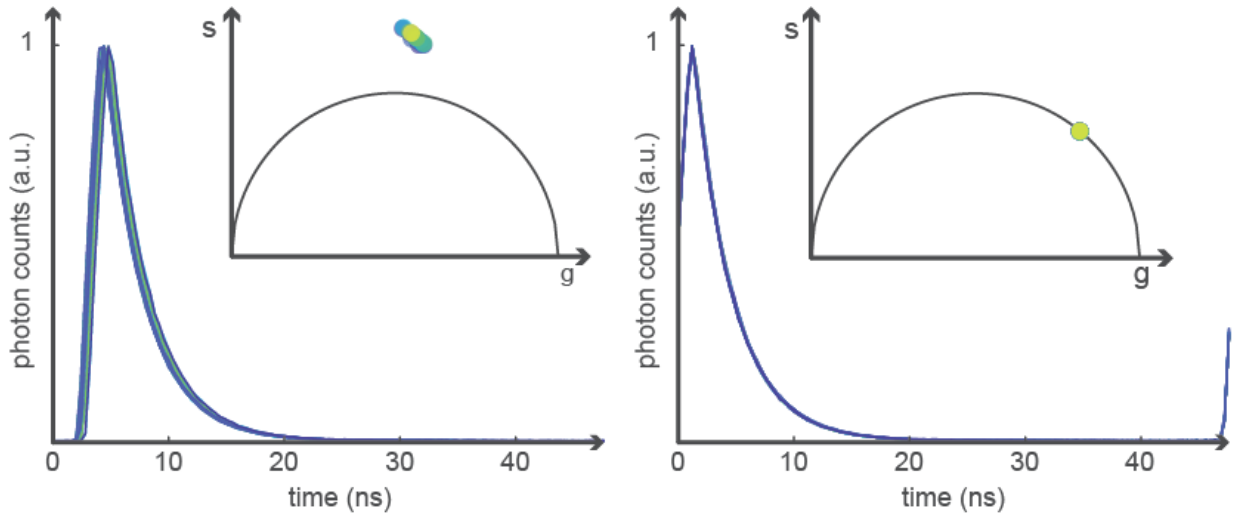

Suppl. Fig. 2 Multi-Channel calibration of the acquisition system. The decays registered by each sensitive element of the SPAD array detector before (left) and after (right) the multi-channel calibration procedure.

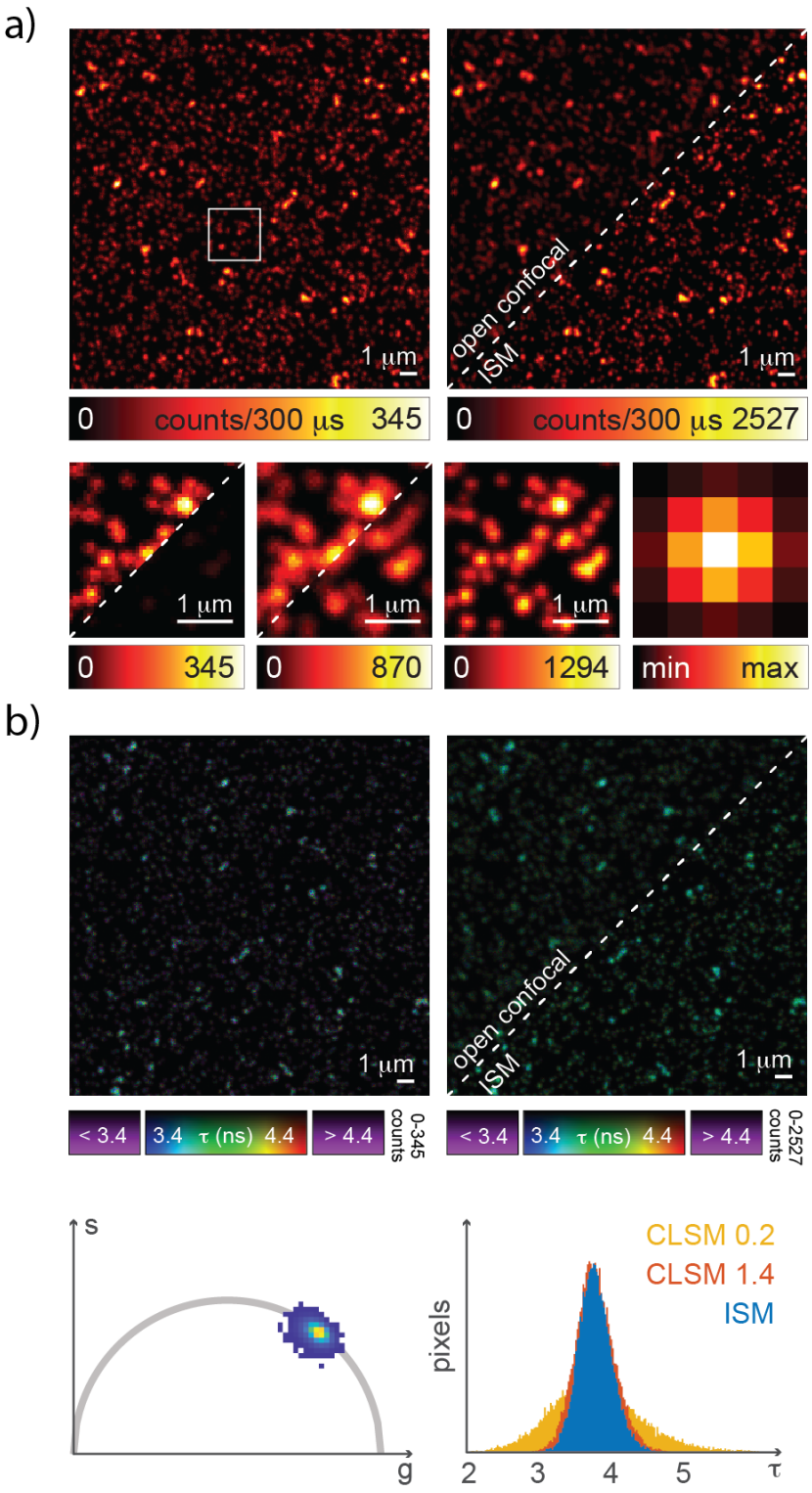

Suppl. Fig. 3 Time-resolved imaging of fluorescent beads. a) Closed confocal (top left, left inset), open confocal (top right, central inset) and ISM imaging (top right, right inset) of fluorescent beads. Right inset: fingerprint matrix. b) Closed confocal (left), open confocal, and ISM lifetime analysis (right) of the same data set in a). Phasor plot for the ISM fluorescence lifetime data set (bottom left) and histograms of the retrieved lifetime values for the different imaging modalities.

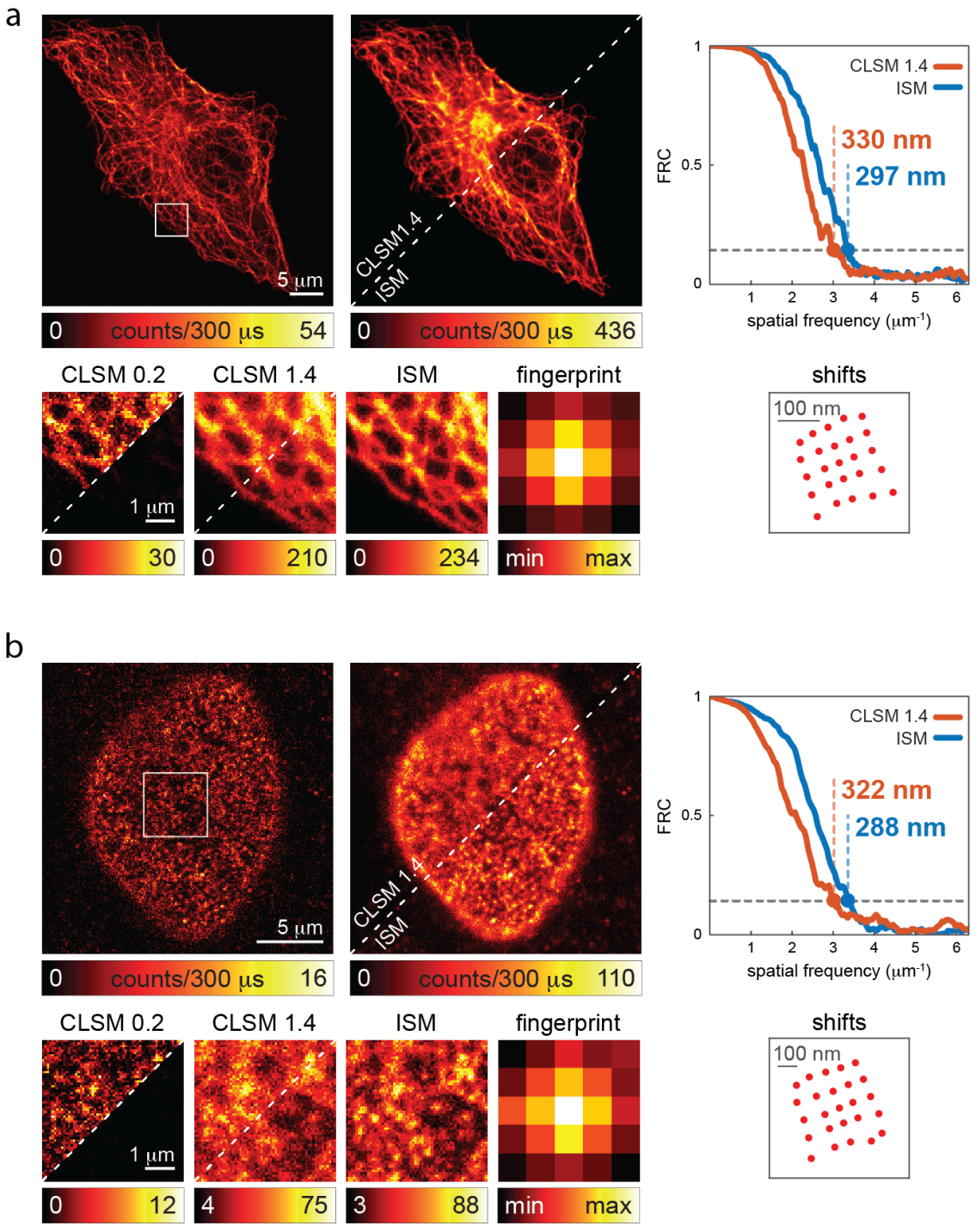

Suppl. Fig. 4 ISM imaging of fixed samples. The panel shows the intensity-based images for the same dataset of Figure 3 (a, b). For imaging of tubulin network (a) and nuclear pore complex (b) the panel shows the close-pihnole image (i.e., central SPAD array element, 0.2. A.U.), the open-pinhole (i.e., the sum of all SPAD array elements, 1.4 A.U.), and the ISM image. The insets shows a detail of the large-field of view image. To highlight the SNR difference between the modality the right corner of the inset are intensity normalised to the ISM counterpart. FRC analysis shows the expected increase in spatial resolution of the ISM result compared to the open-pinhole image. Fingerprint and shift-vectors are also reported.

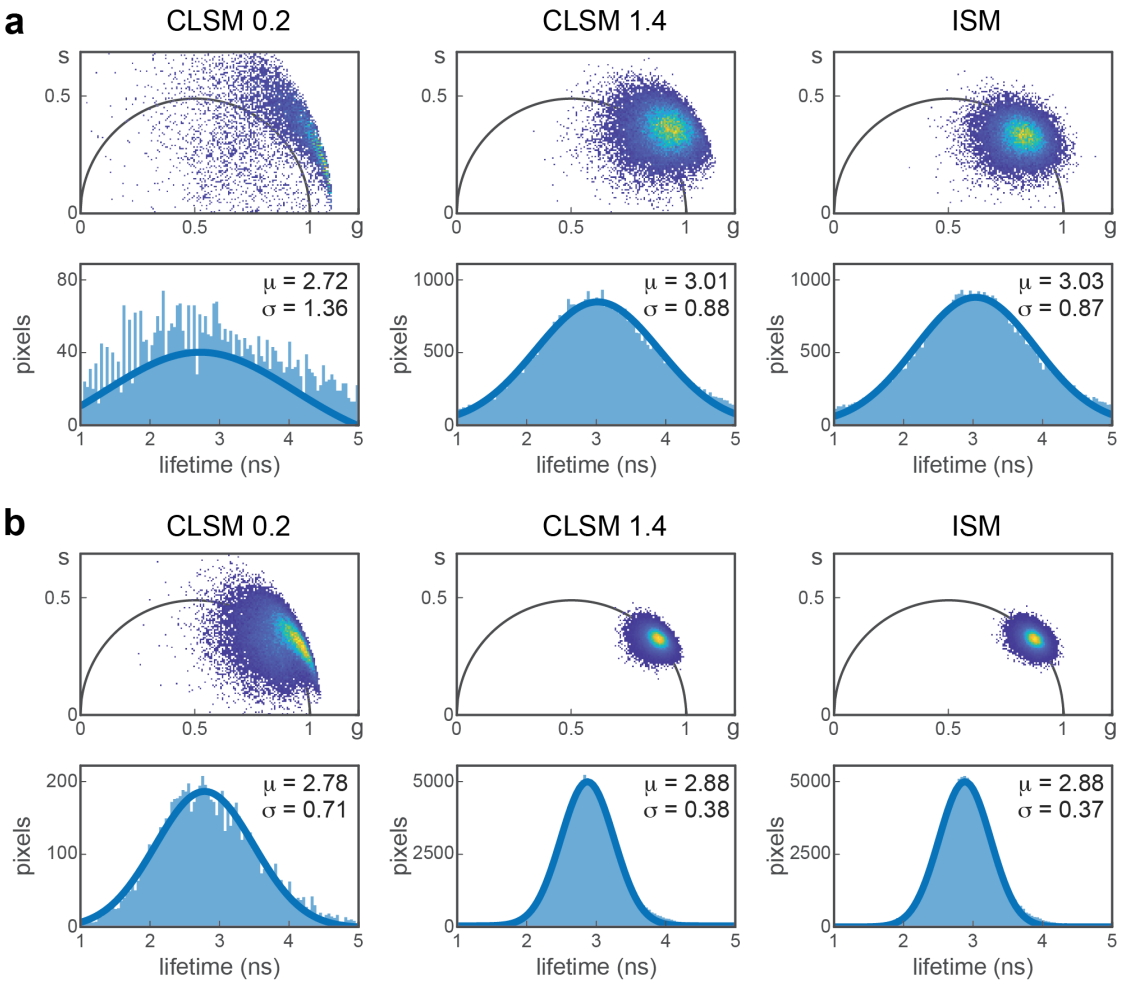

Suppl. Fig. 5 Fluorescence Lifetime histograms and phasors for fixed cells. Phasors (top row) and histograms of the fluorescence lifetime values (bottom row) for the nuclear-pore complex (a) and the tubulin network (b) samples, shown in Fig. 3 of the manuscript. The shown phasors are calculated from the pixels whose photon counts are higher than 20% of the peak of the corresponding image. We fitted the lifetime histograms to a Gaussian model (blue curve); the related mean (μ) and standard deviation (σ) values are reported in nanoseconds. Because of the higher SNR of open-pinhole and ISM images compared to the close-pinhole images, the related fluorescence lifetime values show a narrower distribution, revealed by the narrower histograms and phasor clouds.

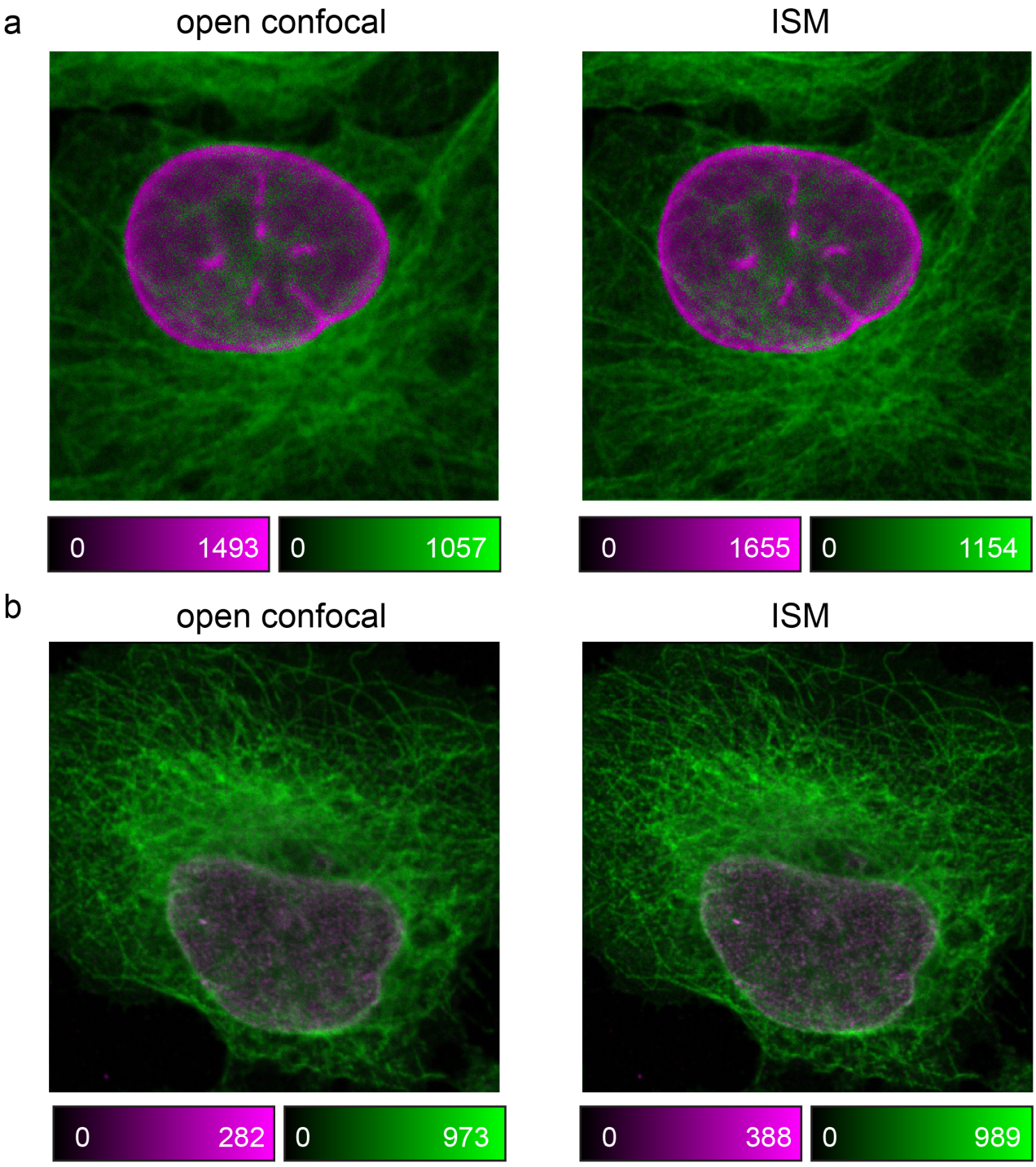

Suppl. Fig. 6 Confocal and ISM multi-color images. Enlarged version of the multi-color images enabled by the lifetime unmixing and pulse interleaving approaches, from Figure 4 of the manuscript.

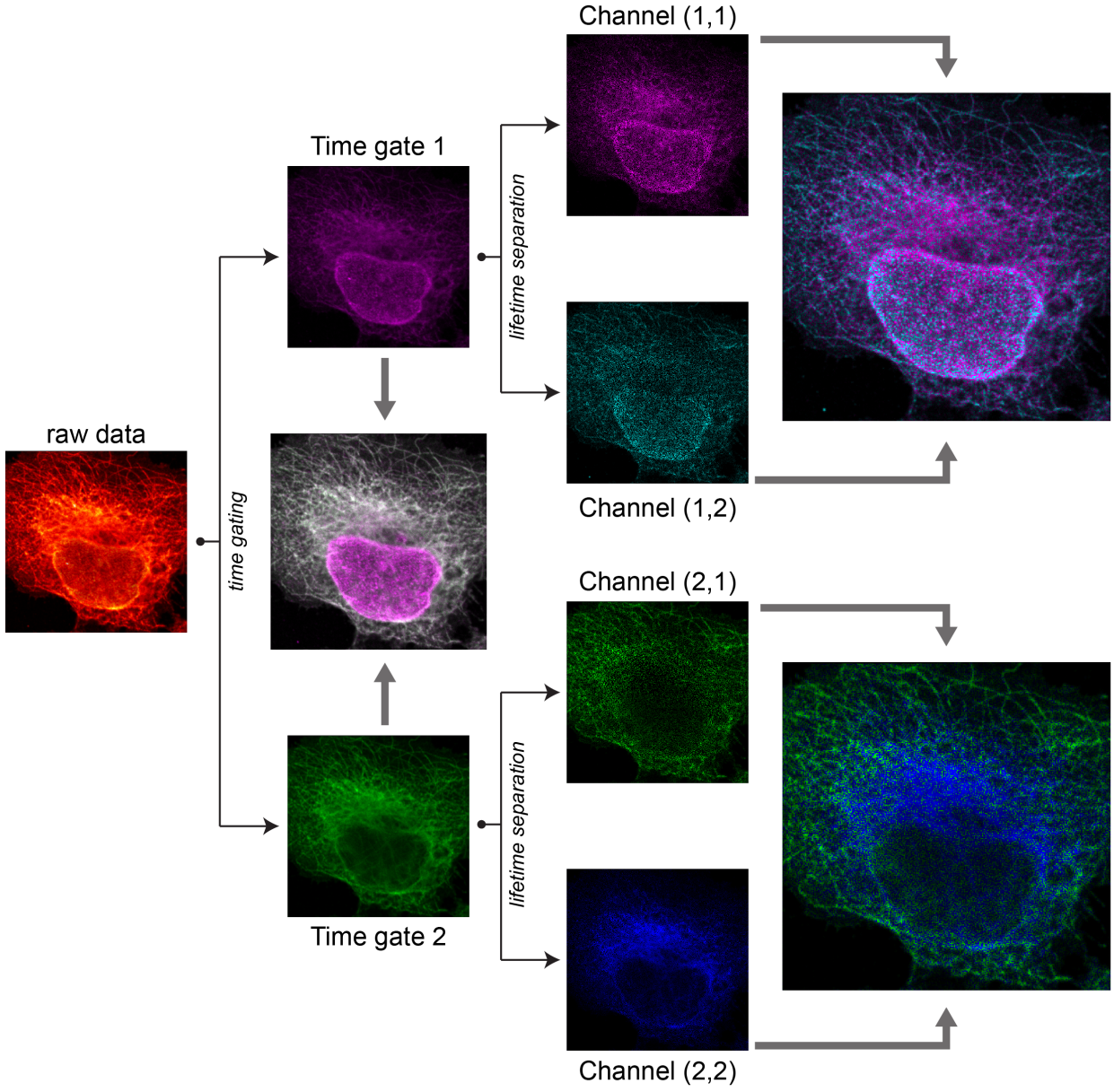

Suppl. Fig. 7 Lifetime unmixing in the PIE experiment. Workflow of channel separation through time-gating. We tried to separate the contribution of each fluorophore from each time window using the lifetime unmixing. However, the two dyes have a similar lifetime, compromising the result. The failure of this approach is clear from the cross-talk of the generated images. This figure show that multi-color imaging with similar absorption spectra and lifetime is feasible only with the additional information provided with pulsed-interleaved excitation (Fig. 4 of the manuscript).

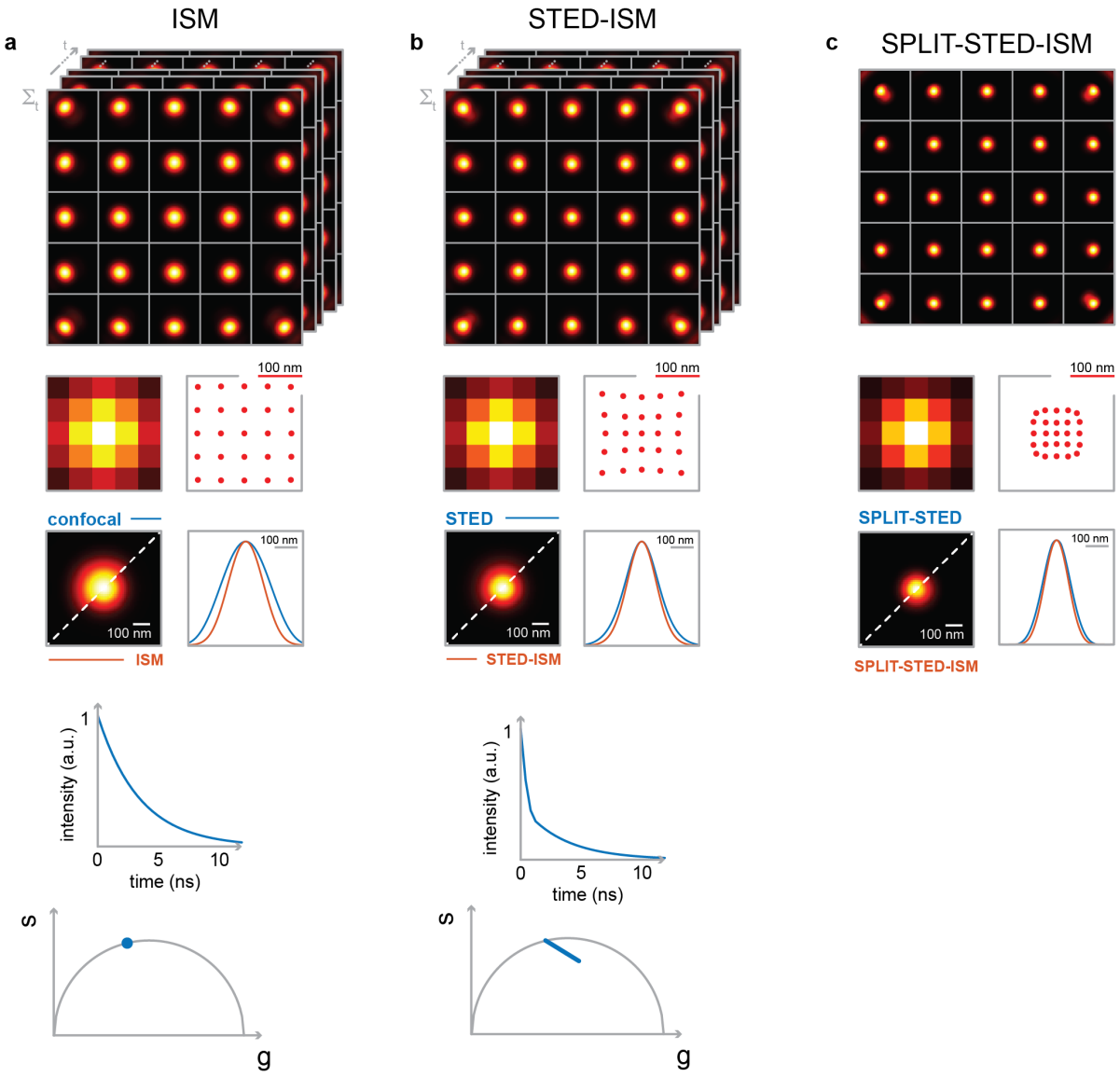

Suppl. Fig. 8 SPLIT-STED-ISM simulations. Simulations of the 5D raw (a) confocal and (b) STED photon-counts map $i(\mathbf{x}_s, \mathbf{x}_d, t)$ recorded by the system when imaging a point source. Top row: representation of the time-dependent PSF for each sensitive element of the detector array. Second row: fingerprint matrix and shift-vectors obtained by integrating each PSF in time. Third row: comparison between (a) raw confocal and ISM or (b) raw STED and STED-ISM. Bottom row: temporal decay of the cumulative PSF, obtained summing all the time-dependent PSFs over $\mathbf{x}_s$ and $\mathbf{x}_d$ (left); phasor representation of the cumulative PSF obtained summing over $\mathbf{x}_d$ only (right). (c) Top: the $i(\mathbf{x}_s, \mathbf{x}_d, t)$ results of the SPLIT approach applied on the raw STED photon-counts map $i(\mathbf{x}_s, \mathbf{x}_d, t)$ in (b). Second row: corresponding fingerprint matrix and retrieved shift-vectors. Third row: comparison with the SPLIT and SPLIT-ISM results – obtained by summing and performing adaptive pixel reassignment, respectively.

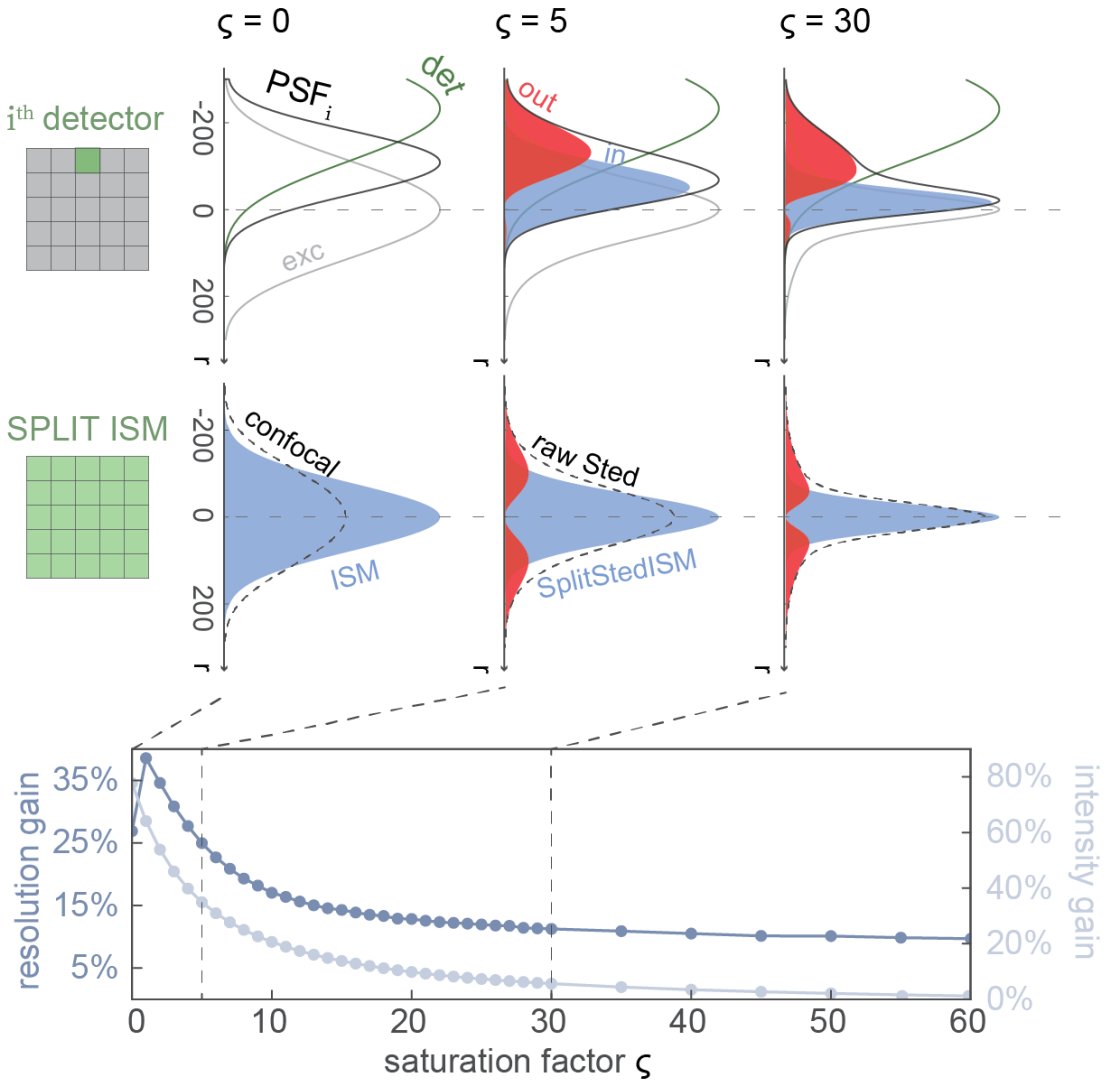

Suppl. Fig. 9 Resolution and intensity gain of SPLIT-STED-ISM imaging. Top row: excitation, detection and effective PSFs of a later detector, displayed for increasing STED saturation factors. In the central and right columns, the high- (blue) and low- (red) resolution contributions are also displayed, as obtained by applying the SPLIT approach. Central row: effects of the adaptive pixel reassignment approach on confocal (left) and STED (center, right) imaging. The ISM (left) or SPLIT-STED-ISM results are displayed in blue. In red, the contribution obtained performing the adaptive pixel reassignment on the low-resolution contributions from all the detectors, as obtained by applying the SPLIT approach. Bottom row: resolution gain – as reported by the Rayleigh value – and intensity gain of the SPLIT-STED-ISM with respect to the raw STED counterpart, with increasing STED saturation factor. The first data point is obtained considering the ISM result and the raw confocal counterpart. The Rayleigh resolution value is obtained using the following strategy: (i) computing the PSF for two point sources at increasing center-to-center distance; (ii) computing the contrast curve as a function of the center-to-center distance. The contrast is defined as $(max - lmin)/max$, where max is the peak value of the intensity line profiles of the two neighbouring objects, and $lmin$ is the value of the local minimum between the two peaks.[6] The Rayleigh resolution is the center-to-center distance for which the contrast reaches the Rayleigh value of 0.26.

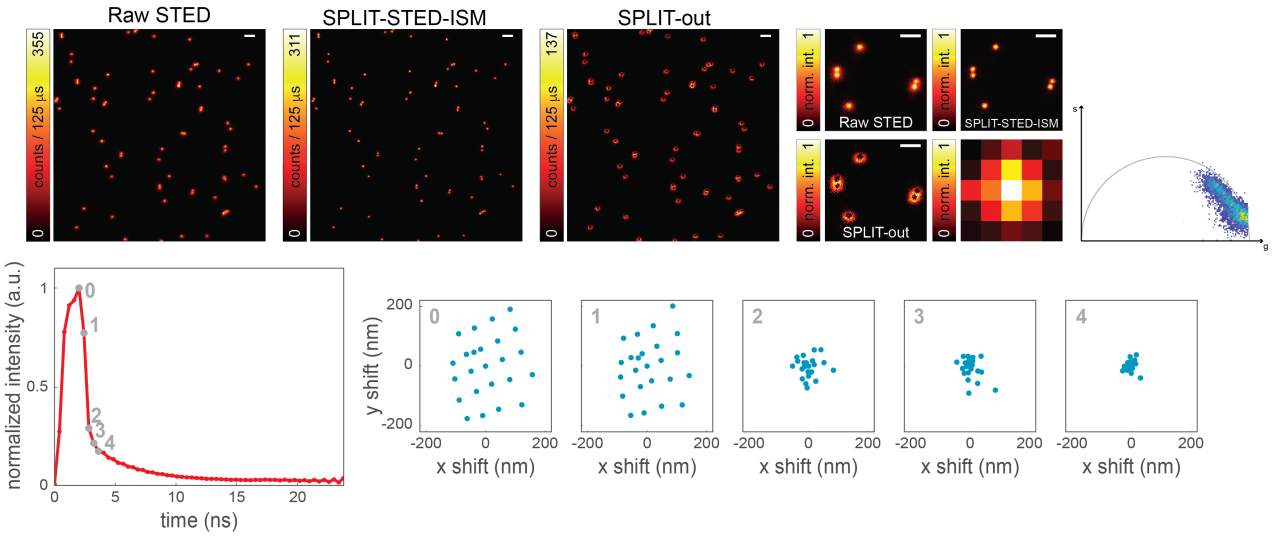

Suppl. Fig. 10 Raw STED and SPLIT-STED-ISM imaging of fluorescent beads. Side-by-side comparison of the Raw STED, the SPLIT-STED-ISM and the SPLIT-out images. The SPLIT approach applied the 5D raw STED photon-counts map $i(\mathbf{x}_s, \mathbf{x}_d, t)$ generates two sets of images $i(\mathbf{x}_s, \mathbf{x}_d)$: (i) the SPLIT set, on which we used the APR method to achieve the final SPLIT-STED-ISM result; and (ii) the SPLIT-out set, that we integrated over $\mathbf{x}_d$ to generate the SPLIT-out image. Right: phasor plot of the raw STED measurement. Bottom, left: temporal decay obtained by integrating the STED photon-counts map $i(\mathbf{x}_s, \mathbf{x}_d, t)$ over $\mathbf{x}_s$ and $\mathbf{x}_d$. Bottom, right: the shift-vectors for the STED photon-counts map $i(\mathbf{x}_s, \mathbf{x}_d, t_i)$ at increasing delays from the depletion event, as retrieved by the adaptive pixel reassignment algorithm. $t_0 = 0$ ns, $t_1 = 0.4$ ns, $t_2 = 0.8$ ns, $t_3 = 1.2$ ns, $t_4 = 1.6$ ns. Image format: 500 x 500 pixels; details format: 100 x 100 pixels; pixel size: 40 nm; excitation power: 3 μW; STED power: 87.5 mW.

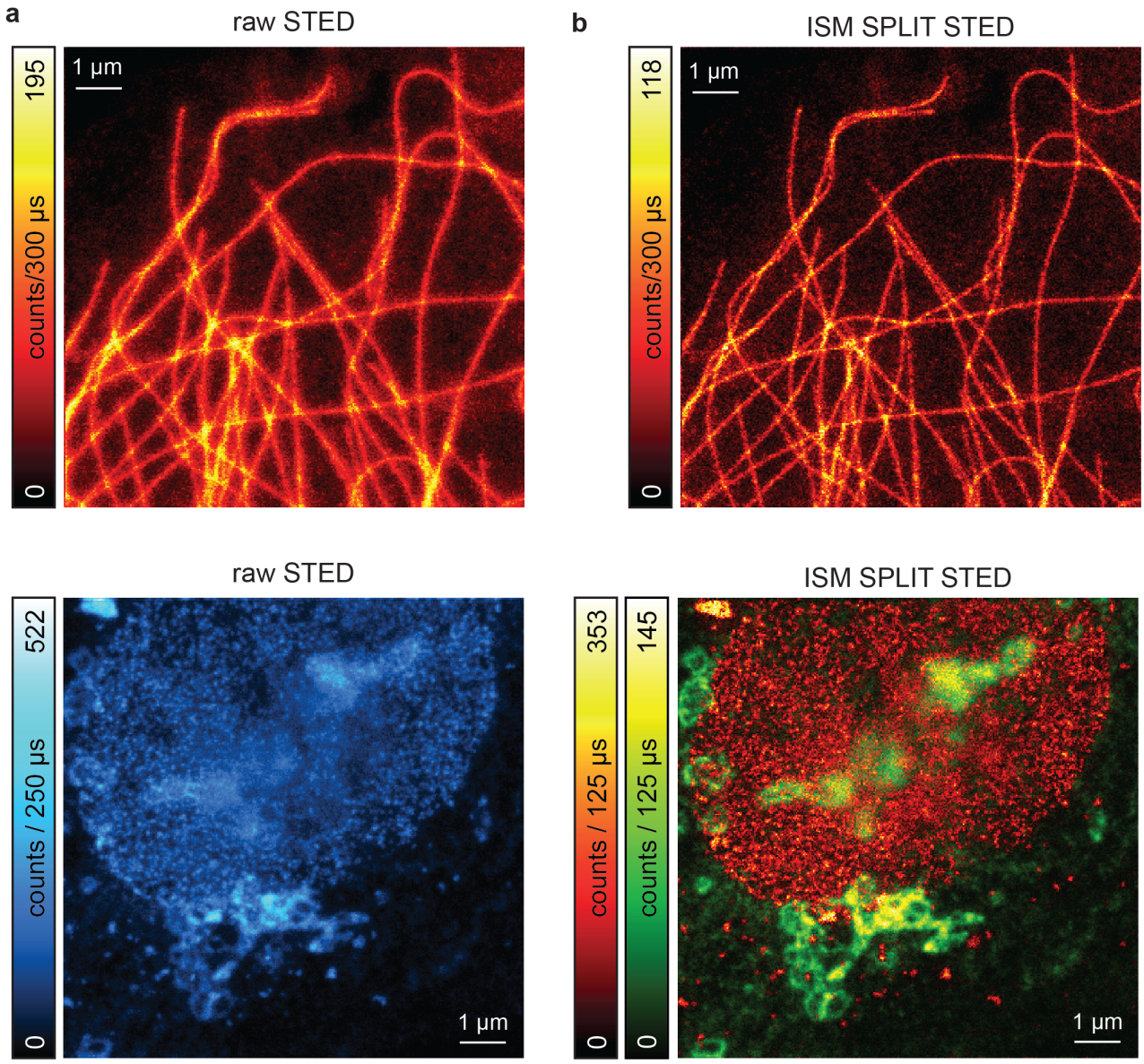

Suppl. Fig. 11 SPLIT-STED-ISM Images. Enlarged version of the panel 5 of the manuscript.

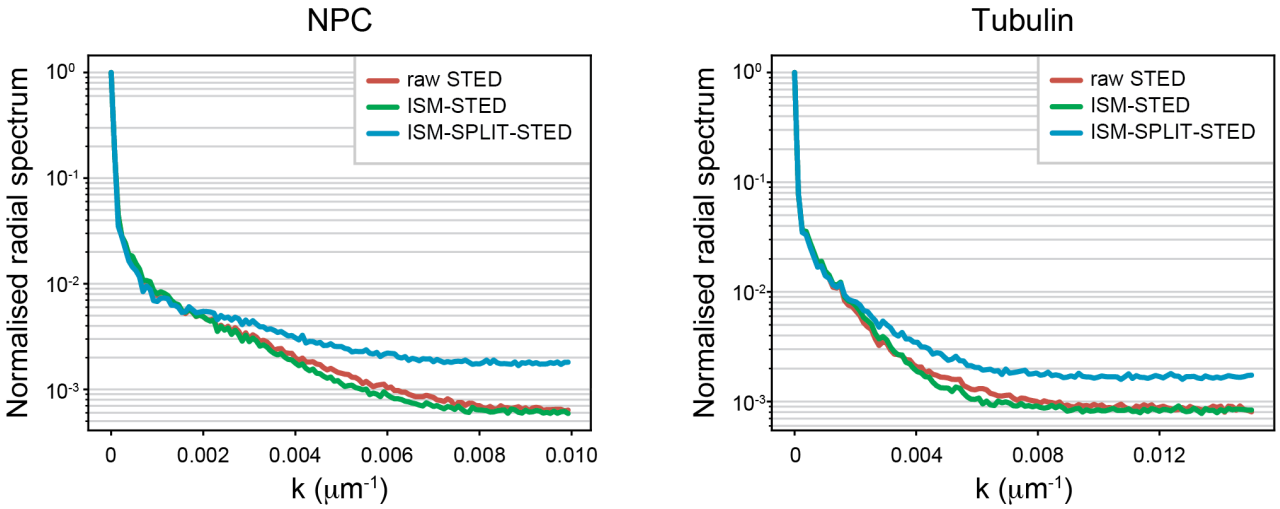

Suppl. Fig. 12 Radial spectrum analysis of raw STED, STED-ISM and ISM-SPLIT-STED datasets. Normalized radial spectra of the nanoscopy image of nano-pore complexes (left) and of tubulin filaments (right), shown in the Suppl. Fig. 11. The spectra of raw STED and STED-ISM do not differ much, as expected from the theory.[7] In contrast, the ISM-SPLIT-STED spectra show an enhancement of high-frequencies, which indicates an increase in lateral resolution and a suppression of low-frequency background.

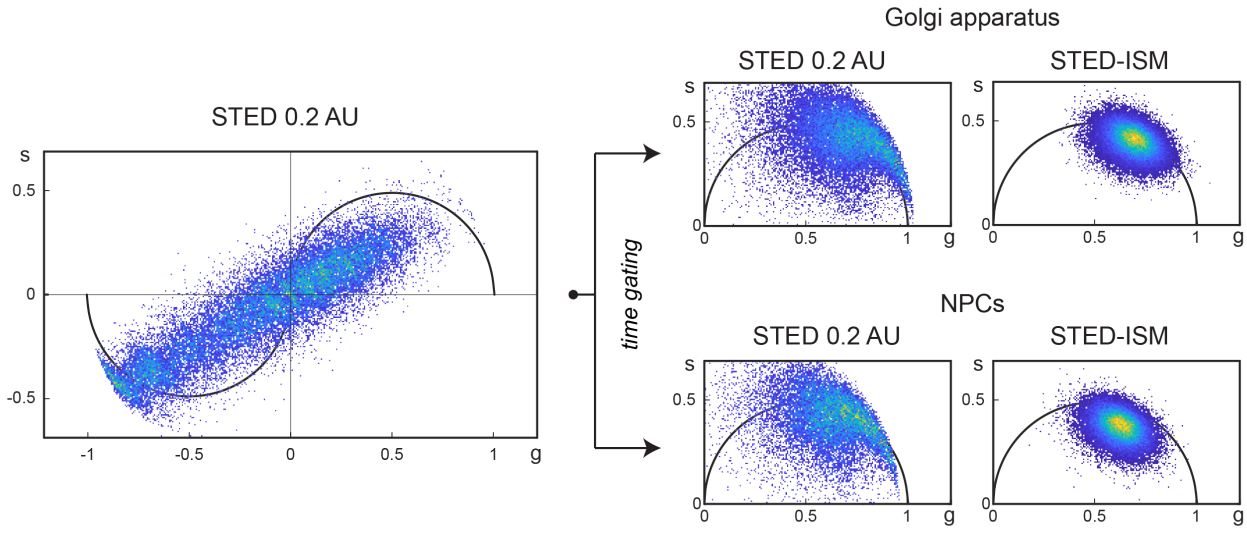

Suppl. Fig. 13 Phasor analysis of the STED data-set. Phasor before (left) and after (right) separation of the data-set in two channels by time gating. Same data as per Fig. 5b. Phasors from the closed-pinhole STED and STED-ISM reconstruction are reported.

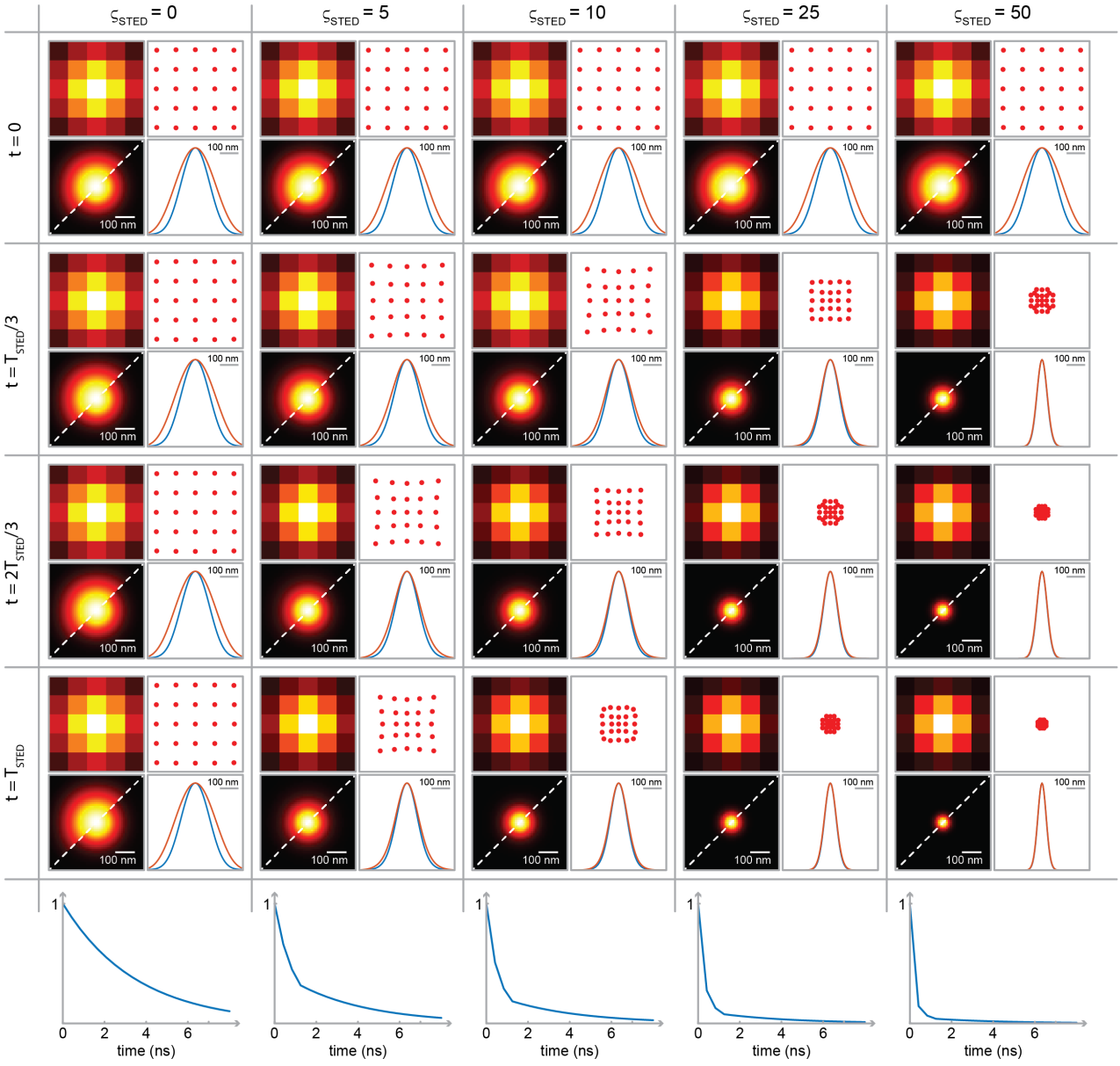

Suppl. Fig. 14 Simulations of time-dependent confocal, raw STED and STED-ISM PSFs. Simulation of the PSFs of a microscope equipped with a detector array (from top to bottom) at different times from the excitation event ($t = 0$) and (from left to right) for increasing STED beam saturation intensities. In each cell: fingerprint matrix describing the distribution of photons on the detector array (top left); shift-vectors retrieved by the adaptive pixel reassignment algorithm (top right); comparison between the open-pinhole (i.e., the sum of all SPAD array elements, 1.4 A.U.) and the STED-ISM PSF (bottom left), and the related line profiles (bottom right). Bottom row: temporal decay of the cumulative PSF for increasing STED saturation factors, obtained by summing all the time-dependent PSFs over $\mathbf{x}_s$ and $\mathbf{x}_d$. Parameters for the simulation: excitation wavelength: 646 nm; depletion wavelength: 775 nm; emission wavelength: 669 nm; STED pulse duration: 1.25 ns; fluorescence lifetime: 3.5 ns.

References

1 M. Castello, G. Tortarolo, M. Buttafava, *et al.*, "A robust and versatile platform for image scanning microscopy enabling super-resolution FLIM," *Nat. Methods* **16**(2), 175–178 (2019).

2 R. A. Colyer, C. Lee, and E. Gratton, "A novel fluorescence lifetime imaging system that optimizes photon efficiency," *Microscopy Research and Technique* **71**(3), 201–213 (2008).

3 L. Lanzanò, I. Coto Hernández, M. Castello, *et al.*, "Encoding and decoding spatio-temporal information for super-resolution microscopy," *Nat. Commun.* **6**, 6701 (2015).

4 I. C. Hernández, L. Lanzanò, M. Castello, *et al.*, "Improving multiphoton STED nanoscopy with separation of photons by LIfetime tuning (SPLIT)," in *Multiphoton Microscopy in the Biomedical Sciences XVIII*, A. Periasamy, P. T. So, X. S. Xie, *et al.*, Eds., SPIE (2018).

5 G. Tortarolo, Y. Sun, K. W. Teng, *et al.*, "Photon-separation to enhance the spatial resolution of pulsed STED microscopy," *Nanoscale* **11**, 1754–1761 (2019).

6 G. Vicidomini, G. Moneron, K. Y. Han, *et al.*, "Sharper low-power STED nanoscopy by time gating," *Nat. Methods* **8**(7), 571–573 (2011).

7 G. Tortarolo, A. Zunino, F. Fersini, *et al.*, "Focus image scanning microscopy for sharp and gentle super-resolved microscopy," *Nature Communications* **13**(1), 7723 (2022).